Earth and Planetary Science Letters 292 (2010) 325–336

Contents lists available at ScienceDirect

Earth and Planetary Science Letters

journal homepage: www.elsevier.com/locate/epsl

Premelting polymerization of crustal and mantle fluids, as indicated by the solubility of albite + paragonite + quartz in H_2O at 1 GPa and 350–620 °C

Craig E. Manning *, Angelo Antignano [1], Heather A. Lin [2]

Department of Earth and Space Sciences, University of California, Los Angeles, CA, 90095-1567, USA

ARTICLE INFO

Article history:
Received 6 August 2009
Received in revised form 7 January 2010
Accepted 27 January 2010
Available online 1 March 2010

Editor: L. Stixrude

Keywords:
fluids
fluid–rock interaction
experimental petrology
granite petrogenesis

ABSTRACT

The composition and structure of dissolved silicates in model crustal and upper-mantle fluids was assessed by measuring the solubility of the assemblage albite + paragonite + quartz in H_2O from 350 to 620 °C, at 1 GPa. Natural, low albite and quartz were equilibrated with H_2O; paragonite grew in all experiments due to incongruent dissolution of albite + quartz. Melting occurred at 635 ± 5 °C. Solute concentrations at subsolidus conditions were determined by analysis of quenched fluids or mineral weight-loss and mass balance. Bulk solubility of the mineral assemblage increased from ~1 to ~8 oxide wt.% with rising temperature. Si, Al, and Na all increase in concert. The solutions were slightly peralkaline, and possess Si/(Na + Al) ≫ 1.5 (molar) at all conditions studied. Extrapolated thermodynamic data were used to predict solubility at the conditions investigated experimentally. Calculated solubility agreed with that measured from 350 to ~500 °C; however, above 500 °C, the calculations underpredict solubility to an increasing degree as the hydrothermal melting point is approached. The excess measured solubility points to increasing abundance of aqueous Si, Al–Si, and Na–Al–Si polymers. Polymerized solutes predominate in all near-solidus solutions, rising to >80% of total dissolved solids at the melting point. The observations support a conceptual model in which, as the temperature of the system rises isobarically at 1 GPa, the silicate components dissolved in the aqueous phase begin to polymerize significantly within ~100 °C of the melting point. The polymerized solutes may facilitate condensation of more polymerized hydrous silicate liquid at the hydrothermal melting point. From the perspective of isobaric cooling, the fluid crossing the solidus retains Na–Al–Si–O clusters or fragments that are less polymerized than those which comprised the melt, but more polymerized than has previously been inferred for the aqueous phase. The high concentrations of Na, Al, and Si in the form of polymeric clusters will yield substantial mass transfer by near-solidus metamorphic and magmatic fluids in the crust and mantle, and likely promote dissolution, transport and precipitation of nominally insoluble, refractory rock components.

1. Introduction

Water plays an important role in crustal and mantle processes through its dramatic lowering of melting temperatures and its ability to transport mass. In simple silicate–H_2O systems, the hydrothermal melting temperature at a given pressure represents the point of maximum water content of a magma coexisting with minerals, and maximum solubility of minerals in the H_2O-rich vapor phase (e.g., Hack et al., 2007). With further rise in temperature in the H_2O-rich portion of such systems, the silicate liquid and aqueous vapor approach one another in composition, becoming fully miscible when the critical curve is reached. The positions of geologically relevant critical curves and their intersections with hydrothermal melting curves have received wide attention due to their possible importance for mass transfer in high pressure environments (e.g., Paillat et al., 1992; Shen and Keppler, 1997; Bureau and Keppler, 1999; Stalder et al., 2000; Manning, 2004; Kessel, et al., 2005; Mibe et al., 2007; Hermann and Spandler, 2008). While the structure of subcritical hydrous silicate magmas is relatively well understood, substantially less is known about the behavior of the aqueous phase at elevated pressures near the solidus. Manning (2004) noted that the continuous compositional variation displayed by supercritical melt–H_2O systems requires that aluminosilicate components be accommodated in H_2O via progressive solute polymerization. Polymerization of aqueous silicates has now been reported in a range of simple systems (Mysen, 1998; Zotov and Keppler, 2000, 2002; Newton and Manning, 2002, 2003, 2008; Manning, 2007; Mibe et al., 2008). A key feature of this process is that, at supersolidus temperature (T), closure of the miscibility gap in binary silicate–H_2O systems requires that polymerization extent must increase with rising T. However, it remains unclear where significant polymerization of multicomponent

* Corresponding author.
E-mail addresses: manning@ess.ucla.edu (C.E. Manning), angelo.antignano@exxonmobil.com (A. Antignano), heather_lin@golder.com (H.A. Lin).
[1] Current address: Exxon Mobil Corporation, P.O. Box 4778, Houston, TX, 77210-4770, USA.
[2] Current address: Golder Associates, 200 Century Suite C, Mt. Laurel, NJ, 08054, USA.

0012-821X/$ – see front matter © 2010 Elsevier B.V. All rights reserved.
doi:10.1016/j.epsl.2010.01.044

aqueous silicate components begins — is it limited to high *T*? Or does it begin well below hydrothermal melting?

This study addressed these questions through experimental investigation of the solubility of albite + paragonite + quartz in H_2O at 1 GPa, from 350 °C to the hydrothermal melting temperature at 635°. This mineral system was employed because albite–H_2O and albite–quartz–H_2O have been used widely as models of melting and metasomatism in the continental crust (e.g., Burnham, 1975; Anderson and Burnham, 1983). By focusing on the isobaric solubility change as temperature increased to the melting point, the experiments probed links between solidus proximity, mineral solubility, and the nature of the solutes. The results provide new insights into the structure and metasomatic capabilities of crustal fluids.

2. Methods

Three types of experiment were conducted depending on temperature and goal: fluid-extraction experiments, weight-loss experiments, and hydrothermal–melting experiments. Each type of run used low albite from Amelia Courthouse (0.29 wt.% K_2O, Kracek and Neuvonen, 1952) and high-purity Brazilian quartz (Manning, 1994). We used a piston-cylinder apparatus with 2.54 cm NaCl–graphite assemblies (Manning, 1994; Manning and Boettcher, 1994). Temperature was controlled with Pt–$Pt_{90}Rh_{10}$ thermocouples, with no correction for the effect of pressure on emf (±3 °C accuracy). Pressure was maintained at 1.00 ± 0.02 GPa using a Bourdon-tube Heise gauge. Quenching was achieved by cutting the power to the apparatus, which cooled the experiments to below 50 °C within 1 min.

2.1. Fluid-extraction experiments

Fluid-extraction experiments were carried out at low *T* (350–500 °C), where bulk solubilities were modest. This type of run was designed to optimize collection of quench fluid for direct analysis. In these experiments, albite and quartz were loaded with microcrystalline paragonite (synthesized from finely ground Amelia albite, reagent grade Al_2O_3 and H_2O at 0.5 GPa, 400 °C, for 138 h) into 2 mm OD Au capsules. After crimping both ends, the Au capsules were placed with ~70–130 µl nanopure H_2O in a 5 mm OD Pt capsule with a triple-crimped and welded base. The quench-analysis runs were conducted as part of a study on sulfur solubility (Lin, 2001), in which two additional crimped, inner 2 mm OD capsules containing Ag° + Ag_2S and Ni + NiO were also present in the experiments. This means that the experimental solutions also carried minor S (<1 to 18 mmol), Ni (<1 to 22 mmol), and Ag (below detection); however, the presence of these elements does not affect the Na, Al or Si concentrations, based on a comparison of solubilities with and without the buffer assemblages at 0.5 GPa and 350 °C (Lin, 2001). This is sensible because of the low solubilities of Ni, Ag, and S, and their known lack of significant complexing between with Na, Al or Si.

After quenching, the capsules were cleaned ultrasonically in dilute HCl to remove any adhering furnace assembly material, rinsed, then dried and weighed to verify that there was no water loss during the course of the experiment, and then placed in a Teflon extraction vessel with 15 ml of 5% HNO_3. The extraction vessel lid pierces the capsule immersed in the acid solution allowing the solutions to mix and equilibrate for greater than 3 h, generally between 12 and 15 h (Manning and Boettcher, 1994). This ensures that the solution will be extracted in an acid environment to prevent precipitation of dissolved material upon extraction, increases the volume of analyte, and counters matrix effects during solution analysis. The solutions were analyzed on a Jobin Yvon JY70PLUS ICP-AES. Run times were 94–257 h, which was sufficient to attain constant solubility with time based on a study at 0.5 GPa, 350 °C (Lin, 2001).

2.2. Weight-loss experiments

For solubility experiments near the hydrothermal melting temperature (580–620 °C), solubilities were dramatically higher, and there was significant solute precipitation on quenching. Weight-loss experiments are more appropriate at such conditions. Accordingly, our high *T* solubility measurements used techniques similar to those of Antignano and Manning (2008a,b). For each experiment, a single, weighed grain of albite was placed in a 1.6 mm OD Pt tube which was crimped to produce an open inner capsule permitting diffusive penetration of the fluid. The inner capsules were then loaded into 3.5 mm OD Pt outer capsules with ultrapure H_2O and a quartz crystal. All experiments were conducted for 24 h.

After experiments, the outer capsule was punctured, dried and weighed. Due to paragonite formation, the post-run H_2O content was slightly less than that added initially (see below); the latter value was therefore used to calculate solubility. Quartz crystals were removed from the outer capsule. Before weighing, minor adhering quench was removed ultrasonically, taking care to ensure that the quartz grain did not chip or break. The inner capsule was removed, dried, weighed, and opened. The albite grain from the inner capsule was in every case partly coated by delicate micrometer-scale paragonite crystal mats (Fig. 1). The aggregate was placed in an ultrasonic bath to remove the paragonite, and then the cleaned albite crystal was dried at 115 °C and weighed again. This procedure quantitatively removed the paragonite coating (Fig. 1). Inspection of the paragonite mass indicated no loss of albite chips or pieces. Run products were examined optically in oil-immersion mounts, by X-ray diffraction (XRD), and by scanning electron microscopy (SEM). All weighing was carried out on a Mettler M3 microbalance with $1\sigma = 2$ µg, yielding a detection limit for weight changes of 6 µg.

Solubilities were determined by mass balance from the mineral weight changes,

$$\Delta w_j = w_j^{\text{initial}} - w_j^{\text{final}} \quad (1)$$

where Δw_j is the weight change of mineral *j* as determined from the difference in weight before (w_j^{initial}) and after (w_j^{final}) experiment. The sign of Δw_j is positive where a mineral loses weight (dissolves) and negative where weight is gained (grows).

The weight changes of quartz (qz) and albite (ab), Δw_{qz} and Δw_{ab}, were readily determined from the weights of the cleaned product crystals and starting weights, and were always positive because both minerals partially dissolved in the experiments (Table 1). Paragonite (pg) was not present initially, but grew in all experiments, so $w_{pg}^{\text{initial}} = 0$ and Δw_{pg} was negative. However, the paragonite could not be collected for weighing because it formed a fragile coating on albite, so w_{pg}^{final} was instead calculated by mass balance. The weight change of the inner capsule after drying but prior to removal of the albite + paragonite aggregate, Δw_{ic}, is

$$\Delta w_{ic} = w_{ic}^{\text{initial}} - w_{ic}^{\text{final}} \quad (2)$$

Mass balance requires that

$$\Delta w_{ic} = \Delta w_{ab} - w_{pg}^{\text{final}} - w_{quench,ic} \quad (3)$$

which upon rearrangement gives

$$w_{pg}^{\text{final}} = \Delta w_{ab} - \Delta w_{ic} - w_{quench,ic} \quad (4)$$

where $w_{quench,ic}$ is the small but unweighable mass of quench solute in the inner capsule. If $w_{quench,ic}$ is ignored and set to zero, a minimum solubility will be obtained from Eq. (4). However, $w_{quench,ic}$ can be estimated within conservative limits from the requirements of the geometry of the double-capsule assembly employed in the

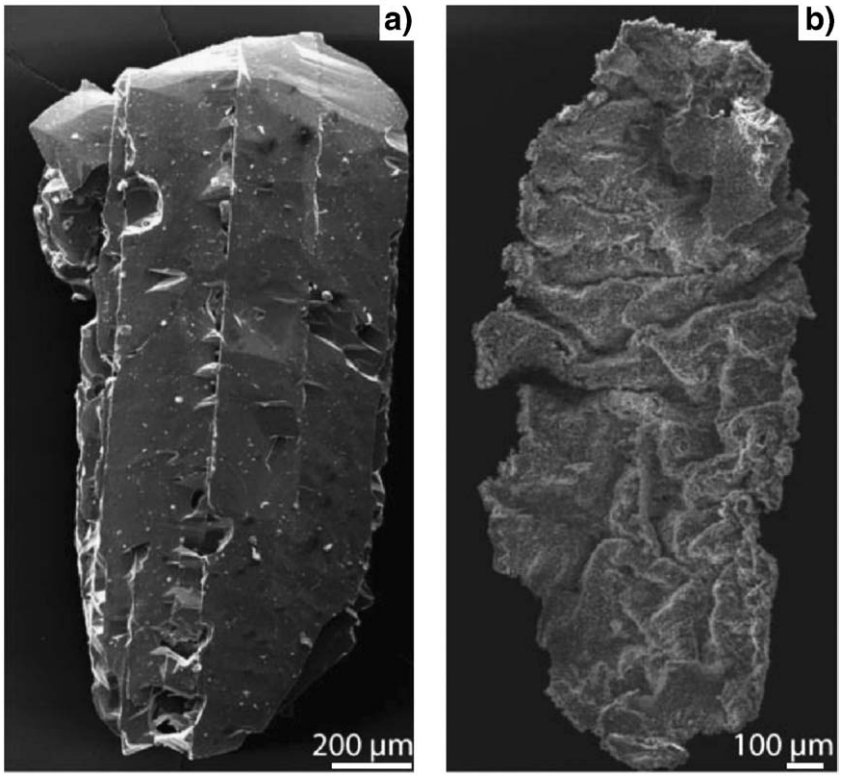

Fig. 1. a. SEM image of partially dissolved albite crystal after experimental dissolution, showing etch pits and channels. The surface has been cleaned of coating paragonite. b. SEM image of paragonite coating removed from albite crystal in (a). Most experiments exhibited smaller, less coherent coatings; all were unweighable because they disaggregated upon contact.

experiments. The scheme for quench correction is outlined in the Supplementary material. Correcting inferred solubility for trapped quench results in a loss of precision; however, the effect is small (quench-corrected solubilities are only $8 \pm 5\%$ greater than if quench mass were neglected) relative to the overall improvement in accuracy.

The measured or calculated mineral weight changes allow calculation of bulk solubility from

$$\text{bulk solubility} = 100\frac{\sum_j \Delta w_j - \Delta w_{pg} f_{pg}}{\sum_j \Delta w_j + w_{H_2O}} \quad (5)$$

Table 1
Experimental results at 1 GPa.

Expt. no.	T (°C)	Duration (h)	Result[a]	H_2O (mg)	Δw_{qz}[b] (mg)	Δw_{ab}[c] (mg)	w_{pg}^{final} (mg)[d,e]	Bulk solubility[e] (wt%)	m_{Na}[e]	m_{Al}[e]	m_{Si}[e]
Quench-analysis experiments											
HL219	350	114	APQV	131.82				0.53 (2)	0.035 (2)	0.0057 (2)	0.065 (2)
HL75	350	118	APQV	71.39				0.30 (2)	0.019 (2)	0.0029 (4)	0.038 (2)
HL77	400	257	APQV	73.55				0.84 (2)	0.056 (2)	0.0124 (8)	0.101 (4)
HL79	450	94	APQV	69.93				0.48 (6)	0.043 (4)	0.0124 (16)	0.047 (8)
HL64	500	119	APQV	74.35				1.81 (6)	0.108 (6)	0.0403 (18)	0.217 (8)
Weight-loss experiments											
AQ3	580	24	APQV	35.835	0.757	1.133	0.173 (77)	4.59 (19)	0.108 (06)	0.083 (17)	0.675 (17)
AQ4	580	24	APQV	35.646	0.683	1.138	0.245 (70)	4.26 (17)	0.104 (05)	0.068 (15)	0.630 (15)
AQ18	600	24	APQV	35.771	0.816	1.694	0.399 (94)	5.62 (22)	0.151 (07)	0.093 (21)	0.834 (21)
AQ19	620	24	APQV	36.852	1.140	2.122	0.197 (139)	7.70 (30)	0.206 (10)	0.178 (30)	1.131 (29)
Hydrothermal melting experiments											
AQ30	630	24	APQV								
AQ34	640	24	PQVL								

[a] Abbreviations: A, albite; P, paragonite, Q, quartz, V, aqueous fluid; L, hydrous silicate liquid.
[b] Weight change of quartz crystal.
[c] Weight change of albite calculated from the difference in weight between the loaded crystal and the cleaned residual albite crystal.
[d] Quench-corrected weight of paragonite calculated assuming effective length ratio L of inner to outer capsule of 0.5 (see text).
[e] Parenthetical numbers are uncertainties in final digits. In quench-analysis experiments, these are propagated 2σ analytical errors; in weight-loss experiments, errors reflect a conservative range of L of 0.3–0.7 (see text) and are used instead of substantially smaller errors in molality of $\sigma_{Na} = 4 \times 10^{-4}$, $\sigma_{Al} = 1 \times 10^{-3}$, and $\sigma_{Si} = 2 \times 10^{-3}$ propagated from weighing uncertainty.

where w_{H_2O} is the mass of H_2O added to the experiment and f_{pg} is the weight fraction H_2O in paragonite, $f_{pg} = \overline{w}_{H_2O}/\overline{w}_{pg}$, where $\overline{w}_{H_2O}$ and $\overline{w}_{pg}$ are the molecular weights of H_2O and paragonite, respectively. Molalities of Na, Al and Si are determined via

$$m_i = \frac{10^6}{w_{H_2O} + \Delta w_{pg} f_{pg}} \left(\sum_j \frac{\nu_i \Delta w_j}{\overline{w}_j} \right) \quad (6)$$

where i denotes the element of interest, ν_i is the number of moles of element i per formula unit in mineral j, $\overline{w}_j$ is the molecular weight of mineral j, and all weights are in milligrams.

2.3. Hydrothermal-melting experiments

Two experiments were conducted at 630 and 640 °C to locate the temperature of hydrothermal melting. All loading methods were the same as in weight-loss experiments; however, run products were not weighed but instead mounted for optical and electron microscopic petrography for phase identification.

3. Results

Results are given in Table 1. In quench-analysis experiments, inspection of the inner capsule indicated the presence of albite, paragonite and quartz after all runs. The minerals were not present in the outer capsule as quench or vapor-transport crystals (cf., Caciagli and Manning, 2003; Tropper and Manning, 2005, 2007; Antignano and Manning, 2008a,b).

In the weight-loss experiments, quartz remained as partially dissolved single crystals, with surfaces that were easily cleaned of minor loose quench material. Residual albite grains exhibited visible etch pits and channels, consistent with partial dissolution (Fig. 1a). Paragonite – confirmed by XRD and consistent with expected stability relations (e.g., Chatterjee, 1972) – formed in all experiments as delicate, irregular mats partly covering albite (Fig. 1b). Paragonite was found only in the inner capsule in association with albite, indicating that it was not a quench product. The presence of paragonite indicates that the assemblage albite + quartz dissolved incongruently at all conditions.

In the two experiments conducted to establish the position of hydrothermal melting of albite + quartz, the appearance of a hydrous silicate melt with paragonite + quartz was readily detected by the disappearance of albite and the presence of a large (>100 μm diameter), vesicular, glassy sphere in the outer capsule. The glass sphere was texturally distinct from much smaller (~1–5 μm) non-vesicular quench spherules. The melting experiments were not reversed; however, the large water–mineral ratio and strong melting signal give confidence that the equilibrium lies at 635 ± 5 °C at 1 GPa.

Combined results of the three sets of experiments are given in Fig. 2. Bulk solubility increases from ~1 wt.% at 350 °C to >8 wt.% at 620 °C. The concentrations of each element also increase with T. Significantly, all solubilities display strong increases within ~100 °C of hydrothermal melting. The solutions are peralkaline (molar Na>Al) and, with one exception, possess excess Si (i.e., molar Si/(Na + Al)> 1.5, the value for albite).

4. Discussion

4.1. Hydrothermal melting temperature of albite + quartz

The 1 GPa hydrothermal melting temperature of 635 ± 5 °C is lower than the values determined by Luth et al. (1964) (659 ± 5 °C, as adjusted by Luth, 1968) and Boettcher and Wyllie (1969) (649 ± 9 °C). The previous studies used synthetic high-albite, whereas we used natural low albite; however, this cannot explain the observation because the high-albite assemblage should melt at lower T (Goldsmith and Jenkins, 1985). Instead, the discrepancy is likely due to the large ratio H_2O to solids, which leverages more accurate detection of melting in the present experiments. It is also possible that there was a failure to nucleate stable paragonite in previous studies, which would yield metastable persistence of albite + quartz in favor of a more aluminous silicate liquid. It should be noted however that the difference among all studies is small.

4.2. Incongruent dissolution of albite + quartz

Previous work has established that, in the absence of quartz, albite dissolves incongruently in H_2O (Currie, 1968; Anderson and Burnham, 1983; Stalder et al., 2000; Shmulovich et al., 2001). The present investigation shows that albite also dissolves incongruently in H_2O in the presence of quartz. Taken together, studies of solutes dissolved in H_2O in equilibrium with albite, with or without quartz, show that they are consistently Si-enriched and Al-depleted relative to albite over a wide range of P and T.

4.3. Comparison to calculated solubility

4.3.1. Computational approach

The isobaric rise in solubility with increasing temperature reflects the increasing stability of aqueous species relative to the crystals with which the aqueous solution is equilibrated. It is of interest to identify the aqueous species responsible for this behavior by calculating species abundances from thermodynamic data. This approach is most efficiently pursued by selecting an initial, simple set of species, and then using trial calculations to guide the identification of additional species that must also be considered because their presence is required in significant concentrations. In the presence of H_2O, the assemblage albite + paragonite + quartz fixes the pH at values greater than acid–base neutrality. We therefore adopt an initial set of eleven species, which includes five ionic species (H^+, OH^-, Na^+, AlO_2^- and $HSiO_3^-$) and six neutral species ($HAlO_{2,aq}$, $NaOH_{aq}$, $NaAlO_{2,aq}$, $NaHSiO_{3,aq}$, $SiO_{2,aq}$, and $Si_2O_{4,aq}$), where species notation follows Shock et al. (1997) and Sverjensky et al. (1997) except for silica species, for which $SiO_{2,aq}$ denotes the monomer and $Si_2O_{4,aq}$ the dimer (Newton and Manning, 2002, 2003, 2008). Species concentrations can be calculated by writing the equilibria

$$3\underset{\text{albite}}{NaAlSi_3O_8} + 2H^+ = \underset{\text{paragonite}}{NaAl_3Si_3O_{10}(OH)_2} + \underset{\text{quartz}}{6SiO_2} + 2Na^+ \quad (7)$$

$$\underset{\text{albite}}{NaAlSi_3O_8} + 2AlO_2^- + 2H^+ = \underset{\text{paragonite}}{NaAl_3Si_3O_{10}(OH)_2} \quad (8)$$

$$H_2O = H^+ + OH^- \quad (9)$$

$$\underset{\text{quartz}}{SiO_2} + H_2O = HSiO_3^- + H^+ \quad (10)$$

$$HAlO_{2,aq} = H^+ + AlO_2^- \quad (11)$$

$$NaOH_{aq} = Na^+ + OH^- \quad (12)$$

$$NaAlO_{2,aq} = Na^+ + AlO_2^- \quad (13)$$

$$\underset{\text{quartz}}{SiO_2} + NaOH_{aq} = NaHSiO_{3,aq} \quad (14)$$

$$\underset{\text{quartz}}{SiO_2} = SiO_{2,aq} \quad (15)$$

$$2SiO_{2,aq} = Si_2O_{4,aq}. \quad (16)$$

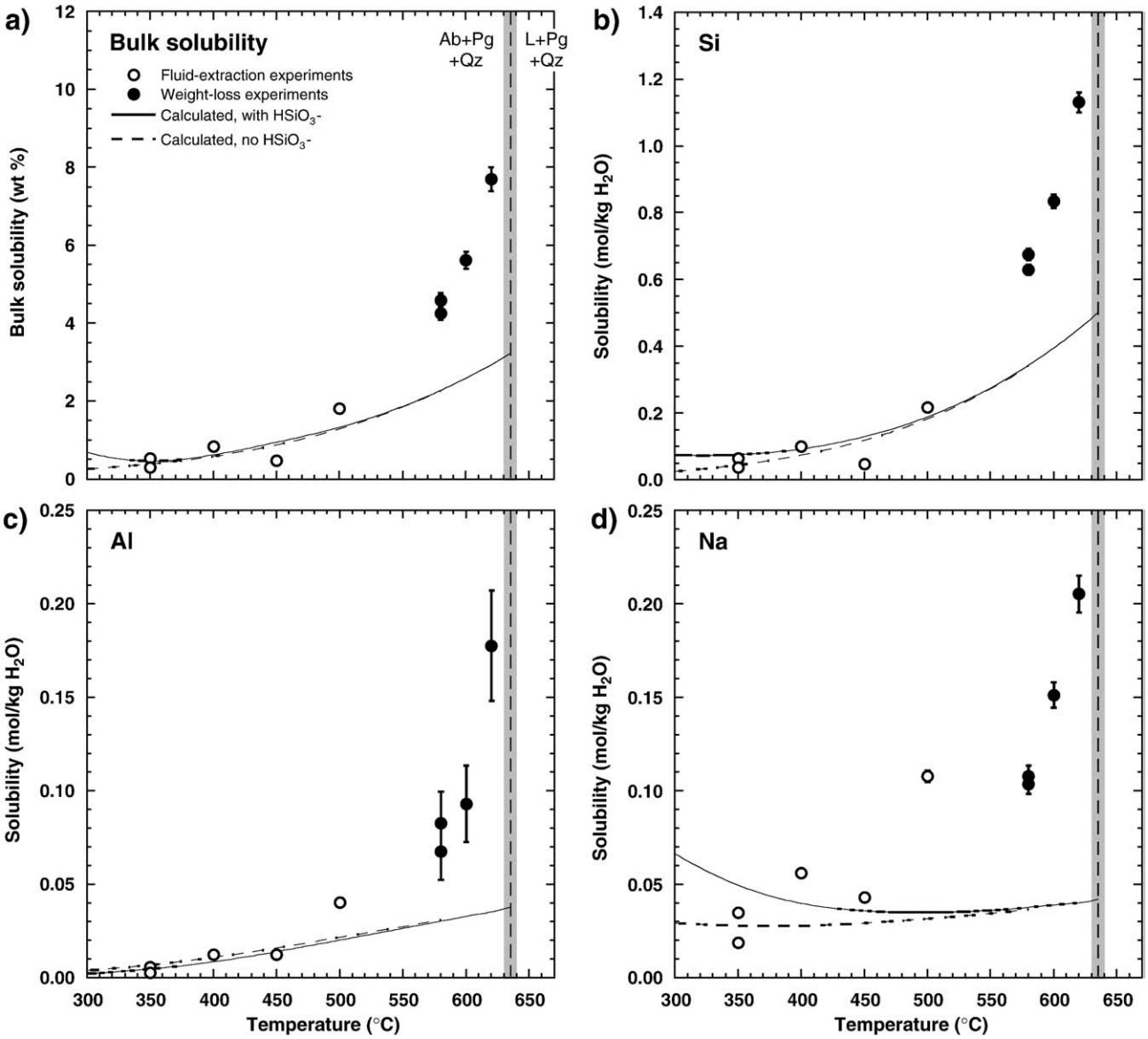

Fig. 2. Temperature dependence of albite + paragonite + quartz solubility in H_2O at 1 GPa, based on fluid-extraction (open circles) and weight-loss (filled circles) experiments. Solubilities include bulk solubility of the assemblage in wt.% (a) and individual elements (molality, b–d). Error bars are shown where larger than symbol size (2σ for fluid-extraction and range between maximum and minimum for weight-loss). The vertical dashed line is drawn at 635 °C, with the range between bracketing experiments shaded. The solid and dashed curves show predicted solubility, with and without consideration of the species $HSiO_3^-$ (see text).

By selecting a standard state of unit activity of pure minerals and H_2O at any P and T, and assuming stoichiometric minerals and $a_{H_2O} = 1$ (see below), the equilibrium constants, K, for Reactions 7–10 are

$$K_7 = \left(\frac{a_{Na^+}}{a_{H^+}}\right)^2 \tag{17}$$

$$K_8 = \left(a_{AlO_2^-} a_{H^+}\right)^{-2} \tag{18}$$

$$K_9 = a_{H^+} a_{OH^-} \tag{19}$$

$$K_{10} = a_{HSiO_3^-} a_{H^+} \tag{20}$$

where a is activity of the subscripted species or phase. In addition, charge balance requires that

$$m_{H^+} + m_{Na^+} = m_{OH^-} + m_{AlO_2^-} + m_{HSiO_3^-} \tag{21}$$

Adopting a standard state for ions of unit activity of the hypothetical 1 m solution referenced to infinite dilution, the concentrations of species can be substituted for activities in Eqs. (17)–(20) using $a_i = \gamma_i m_i$, where γ_i is activity coefficient, which can be computed from a suitable activity model for ions. We use the Güntelberg equation,

$$\log \gamma_i = -\frac{A z_i^2 \sqrt{I}}{1 + \sqrt{I}} \tag{22}$$

where z is the ion charge, I is the ionic strength, and A is a solvent parameter, here assumed to be unity following arguments of Manning (1998, 2007). The Güntelberg equation was used because of its simplicity and success in predicting high-P mineral solubilities in independent studies (Manning, 2007; Wohlers and Manning, 2009). In the Güntelberg equation, activity coefficients are equal for ions of the same absolute charge. Hence, for monovalent ions regardless of charge, Eq. (22) gives the activity coefficient, γ_1, as $\log \gamma_1 = -\sqrt{I} / \left(1 + \sqrt{I}\right)$,

which leads to the following equations for the concentrations of the five ionic species:

$$m_{H^+} = \frac{1}{\gamma_1}\left(\frac{K_8^{-1/2} + K_9 + K_{10}}{1 + K_7^{1/2}}\right)^{1/2} \quad (23)$$

$$m_{OH^-} = \frac{K_9}{\gamma_1^2 m_{H^+}} \quad (24)$$

$$m_{Na^+} = K_7^{1/2} m_{H^+} \quad (25)$$

$$m_{AlO_2^-} = \frac{1}{\gamma_1^2 m_{H^+} K_8^{1/2}} \quad (26)$$

$$m_{HSiO_3^-} = \frac{K_{10}}{\gamma_1^2 m_{H^+}} \quad (27)$$

Upon solution of these equations, the concentrations of the neutral species can be determined. We assume unit activity coefficients for neutral species (e.g., Walther and Helgeson, 1977), which has proven accurate in previous studies of the systems SiO_2–H_2O (Newton and Manning, 2003, 2008), Al_2O_3–SiO_2–H_2O (Manning, 2007) and K_2O–Al_2O_3–H_2O (Wohlers and Manning, 2009). This leads to:

$$m_{HAlO_{2,aq}} = K_{11}^{-1}\gamma_1^2 m_{H^+} m_{AlO_2^-} \quad (28)$$

$$m_{NaOH_{aq}} = K_{12}^{-1}\gamma_1^2 m_{Na^+} m_{OH^-} \quad (29)$$

$$m_{NaAlO_{2,aq}} = K_{13}^{-1}\gamma_1^2 m_{Na^+} m_{AlO_2^-} \quad (30)$$

$$m_{NaHSiO_{3,aq}} = K_{14} m_{NaOH_{aq}} \quad (31)$$

$$m_{SiO_{2,aq}} = K_{15} \quad (32)$$

$$m_{Si_2O_{4,aq}} = K_{16} m_{SiO_{2,aq}}^2 \quad (33)$$

Solutions to Eqs. (22)–(33) require values of the equilibrium constants, which were obtained using SUPCRT92 (Johnson et al., 1992) with thermodynamic data for minerals, H_2O and aqueous species from Helgeson et al. (1978), Haar et al. (1984) and Pokrovskii and Helgeson (1995), except for aqueous silica species (see below). Equilibrium constants for Eqs. (7)–(14) can be calculated only to 500 MPa at 700 °C using SUPCRT92; however, values at the higher P of the present study can be obtained by extrapolation of SUPCRT92 results using the approach of Manning (1998), which is based on the observation that log$K$ of homogeneous equilibria and mineral hydrolysis reactions are effectively linear in $\log\rho_{H_2O}$ above ~300 MPa (e.g., Marshall and Franck, 1981; Marshall and Mesmer, 1984; Mesmer et al., 1988; Anderson et al., 1991). This is illustrated in Fig. 3 for representative equilibria at 600 °C, where it can be seen that the isothermal variation in log$K$ with $\log\rho_{H_2O}$ at 300–500 MPa, illustrated at 50 MPa increments, is highly linear for all equilibria. Isothermal linear fits at ≥300 MPa yield log$K$ values listed in Table 2. Values of log$K$ for Eqs. (15) and (16) were calculated from a linear $1/T$ fit of 1 GPa values of Newton and Manning (2002), and are also given in Table 2.

Using an initial value of $I = 0$, iterative solution of Eqs. (22)–(27) yielded constant I and species concentrations to a level of precision much greater than the experimental data in <10 steps. Based on the results (Table 2), two assumptions required to perform these calculations can be checked. First, our assumption of unit H_2O activity is found to be acceptable, since the minimum mole fraction of H_2O in the calculations (at 635 °C) is 0.990. Second, we ignored the positively charged aluminum species Al^{+3}, $AlOH^{+2}$, and AlO^+. This is supported by calculated pH, which is significantly greater than the extrapolated pK_a for the stepwise dissociation of positively charged aluminate species.

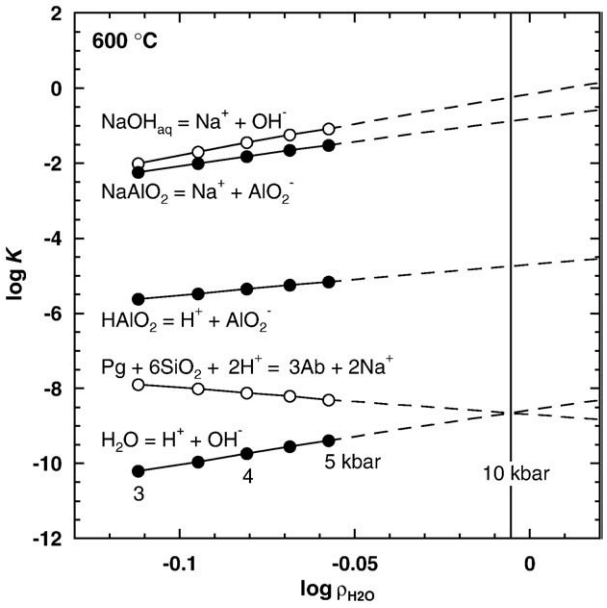

Fig. 3. Variation in log$K$ with log ρ_{H_2O} at 600 °C for selected equilibria. Circles represent values at 0.3–0.5 GPa, at 0.05 GPa increments, calculated using SUPCRT92 using the Haar et al. (1984) equation of state for H_2O. Above 0.3 GPa, calculated log$K$ values are linear within uncertainties (cf., Manning, 1998, 2007). Dashed lines are extrapolations to high ρ_{H_2O} based on linear fits to the 0.3–0.5 GPa values of log$K$ (Table 2). Note that the albite–paragonite–quartz reaction (Eq. 7) is reversed for illustration and comparison of log$K$ behavior.

4.3.2. Calculated vs. observed solubilities

At ≥350 °C, calculated bulk, Si, and Al solubilities increase with increasing T at 1 GPa (Table 2; Fig. 2). In contrast, Na concentration is calculated to have a broad minimum at intermediate T, with only weak increase as the hydrothermal melting T is approached (Fig. 2d). The behavior of Na is strongly controlled by pH, which is calculated to be alkaline at 300 °C (6.7 vs. $pH_{neutral} = 4.4$), but less so at 635 °C (5.9 vs. 4.2). The alkaline pH translates to elevated concentration of deprotonated silica ($HSiO_3^-$) below 450 °C, which in turn leads to high molality of charge-balancing Na^+, the predominant cation at these conditions. This pronounced effect raised concern that thermodynamic properties of $HSiO_3^-$ may be inaccurate. As a check, the calculations were repeated omitting $HSiO_3^-$ (dashed lines, Fig. 2). It can be seen that omission of this species has negligible effect on bulk solubility, except below 350 °C, where slightly lower values are obtained. Accordingly, all subsequent discussion is based on results in which $HSiO_3^-$ was included.

Calculated bulk, Si, and Al concentrations show good agreement with experimentally determined values at 350 °C to ~500 °C, despite moderate scatter in the data (Fig. 2). Measured Na concentrations display significant scatter in fluid-extraction experiments, but the results at 350–450 °C appear to be broadly consistent with calculated concentrations; however, Na concentration determined at 500 °C is much greater than the calculated value. Beginning at ~500 °C, the measured concentrations are higher than those predicted from thermodynamic data for all elements, as well as bulk solubility. Fig. 2 shows that the discrepancy between calculated and measured values grows larger as T increases to the hydrothermal melting point. This conclusion holds regardless of whether the $HSiO_3^-$ species is included in the calculations (Fig. 2).

Table 2
Log*K* values and calculation results at 1 GPa.

		Temperature (°C)								
	Eq. no.	300	350	400	450	500	580	600	620	635
logK values										
$3Ab + 2H^+ = Pg + 6Qz + 2Na^+$	7	10.714	10.208	9.798	9.471	9.199	8.852	8.777	8.697	8.680
$Ab + 2AlO_2^- + 2H^+ = Pg$	8	19.187	18.232	17.436	16.760	16.198	15.501	15.340	15.219	15.117
$H_2O = H^+ + OH^-$	9	−8.783	−8.624	−8.519	−8.443	−8.407	−8.412	−8.408	−8.428	−8.433
$Qz + H_2O = HSiO_3^- + H^+$	10	−8.251	−8.292	−8.382	−8.492	−8.634	−8.910	−8.968	−9.051	−9.067
$HAlO_{2,aq} = H^+ + AlO_2^-$	11	−4.299	−4.273	−4.289	−4.332	−4.403	−4.565	−4.605	−4.659	−4.694
$NaOH_{aq} = Na^+ + OH^-$	12	0.419	0.372	0.318	0.263	0.196	0.056	0.031	−0.019	−0.043
$NaAlO_{2,aq} = Na^+ + AlO_2^-$	13	−0.098	−0.204	−0.302	−0.389	−0.478	−0.635	−0.664	−0.712	−0.738
$Qz + NaOH_{aq} = NaHSiO_{3,aq}$	14	1.286	0.817	0.447	0.100	−0.235	−0.748	−0.864	−0.987	−1.078
$Qz = SiO_{2,aq}$	15	−1.590	−1.365	−1.168	−1.003	−0.868	−0.706	−0.674	−0.644	−0.623
$SiO_{2,aq} = Si_2O_{4,aq}$	16	−0.496	−0.308	−0.149	−0.011	0.108	0.270	0.305	0.339	0.364
Calculation results										
I		0.066	0.049	0.039	0.035	0.034	0.036	0.037	0.037	0.039
γ_1		0.624	0.659	0.683	0.695	0.699	0.694	0.690	0.690	0.685
pH		6.741	6.594	6.470	6.347	6.224	6.034	5.984	5.942	5.916
$\log[H^+]$		−6.536	−6.413	−6.305	−6.189	−6.068	−5.875	−5.823	−5.780	−5.752
$\log[OH^-]$		−1.838	−1.849	−1.883	−1.938	−2.027	−2.220	−2.263	−2.325	−2.352
$\log[AlO_2^-]$		−2.648	−2.341	−2.082	−1.875	−1.720	−1.558	−1.525	−1.506	−1.478
$\log[Na^+]$		−1.179	−1.309	−1.406	−1.454	−1.468	−1.449	−1.434	−1.432	−1.412
$\log[HAlO_{2,aq}]$		−5.295	−4.843	−4.429	−4.048	−3.696	−3.186	−3.065	−2.951	−2.865
$\log[NaOH_{aq}]$		−3.845	−3.892	−3.937	−3.971	−4.003	−4.042	−4.051	−4.061	−4.050
$\log[NaAlO_{2,aq}]$		−4.139	−3.808	−3.517	−3.255	−3.021	−2.690	−2.617	−2.549	−2.481
$\log[SiO_{2,aq}]$		−1.590	−1.365	−1.168	−1.003	−0.868	−0.706	−0.674	−0.644	−0.623
$\log[Si_2O_{4,aq}]$		−3.677	−3.038	−2.485	−2.016	−1.628	−1.143	−1.043	−0.949	−0.882
$\log[HSiO_3^-]$		−1.306	−1.517	−1.746	−1.987	−2.255	−2.718	−2.823	−2.948	−2.986
$\log[NaHSiO_{3,aq}]$		−2.559	−3.076	−3.490	−3.871	−4.238	−4.790	−4.914	−5.048	−5.128
$\log[Na_{total}]$		−1.160	−1.299	−1.397	−1.444	−1.454	−1.423	−1.406	−1.399	−1.375
$\log[Al_{total}]$		−2.633	−2.325	−2.065	−1.854	−1.694	−1.518	−1.480	−1.455	−1.421
$\log[Si_{total}]$		−1.106	−1.118	−1.033	−0.889	−0.725	−0.465	−0.404	−0.344	−0.300
Bulk solubility (wt.%)		0.692	0.634	0.720	0.949	1.326	2.276	2.590	2.935	3.230

Abbreviations: Ab, albite; Pg, paragonite, Qz, quartz. Square brackets indicate molal concentrations. Bulk solubility given as oxides (SiO_2, $AlO_{1.5}$, $NaO_{0.5}$), in wt.%.

4.4. Origin of excess solubility by solute polymerization

The solubility of the assemblage albite + paragonite + quartz in H_2O is substantially greater than predicted once temperature rises to within ~100 °C of hydrothermal melting (Fig. 2), and the excess solubility grows as the melting *T* is approached (Fig. 2). These observations could be explained as (1) an artifact of the different experimental methods used at 350–500 °C vs. 580–620 °C, (2) inaccurate extrapolation of thermodynamic data, or (3) presence of species not included in the calculations. The different experimental approaches are not likely to cause the discrepancy because the combined data sets define coherent trends, despite minor scatter. Moreover, the 500 °C data determined by fluid-extraction indicate that even at this *T*, there is higher measured bulk solubility (due to excess Al and Na) than is calculated. Likewise, failure of the extrapolation scheme with increasing *T* is not likely because the same approach has been used with success at 700 °C, 1 GPa, where measured corundum solubility in H_2O and H_2O–KOH solutions agrees well with calculated values (Tropper and Manning, 2007; Wohlers and Manning, 2009), and excess solubility of all three elements indicates that inaccurate thermodynamic data in one or two species cannot account for the observations.

Instead, the excess solubility within ~100 °C of hydrothermal melting is most simply explained by the appearance of additional dissolved species that were not included in the calculations. The oxide and bulk compositions of these excess species are given in Table 3. From 580 °C to the melting temperature, the missing species are the predominant reservoirs for each of the three elements (Fig. 4). In addition, these species dominate the solute load to an increasing degree as the melting point is approached: from 580 to 620 °C, the element fractions occurring as excess species rise from 48 to 60% Si, 60 to 80% Al, and 64 to 81% Na (Fig. 4).

Because the solubility calculations included all conceivably significant monomers, deprotonated monomers, ions, and simple species, the candidate species that could explain the excess solubility must be polymerized species. Because we considered $NaAlO_{2,aq}$ and $NaHSiO_{3,aq}$,

Table 3
Composition of solute fractions (oxide wt.%).

	580 (°C)	600 (°C)	620 (°C)	635 (°C)
Observed				
$NaO_{0.5}$	0.313	0.443	0.588	0.722
$AlO_{1.5}$	0.367	0.448	0.836	1.051
SiO_2	3.748	4.729	6.274	7.394
Σ	4.428	5.620	7.698	9.167
Excess				
$NaO_{0.5}$	0.199	0.324	0.468	0.595
$AlO_{1.5}$	0.215	0.284	0.662	0.864
SiO_2	1.737	2.421	3.633	4.478
Σ	2.151	3.029	4.763	5.937
Polymerized				
$NaO_{0.5}$	0199	0.324	0.468	0.595
$AlO_{1.5}$	0.215	0.284	0.662	0.864
SiO_2	2.582	3.481	4.944	6.002
Σ	2.996	4.089	6.074	7.461
Unpolymerized				
$NaO_{0.5}$	0.114	0.119	0.120	0.126
$AlO_{1.5}$	0.151	0.164	0.174	0.187
SiO_2	1.166	1.248	1.330	1.391
Σ	1.431	1.531	1.624	1.704

Explanation: excess values reflect the difference between observed and calculated values; polymerized and unpolymerized values are excess and calculated values, except for silica, for which calculated $Si_2O_{4,aq}$ is included with polymerized SiO_2. Values at 635 °C were calculated by extrapolation of polynomial fit in *T*, assuming 0% excess at 500 °C.

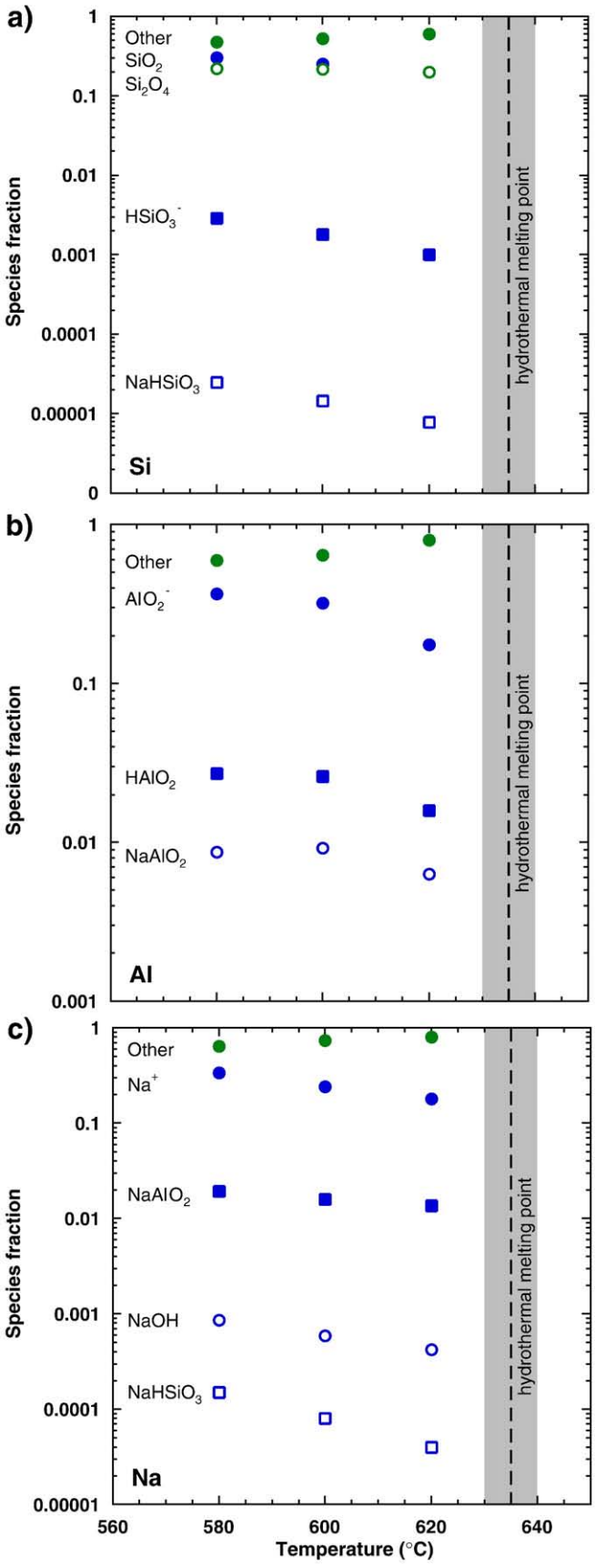

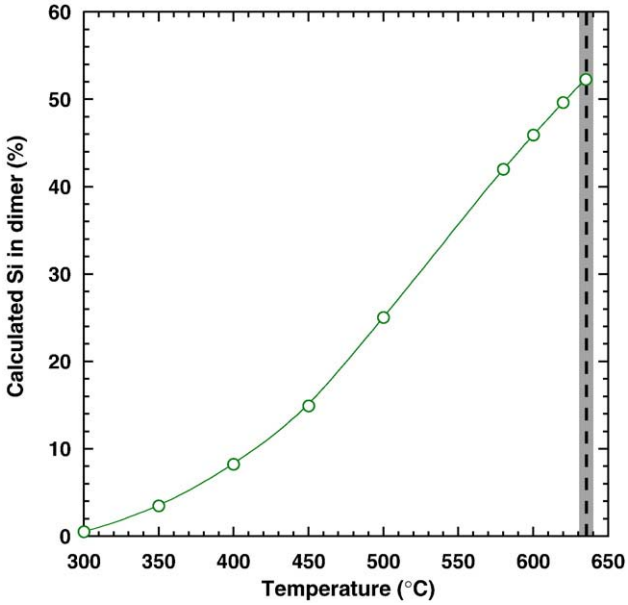

Fig. 5. Isobaric change in the calculated fraction of silica in dimers with temperature. Dimers represent nearly half the total calculated Si in solution within 50 °C of melting; however, even more polymerized species must be present to account for the large excess solubility at these conditions. Melting point as in Fig. 2.

the excess species possess even more complex composition and stoichiometry. To the extent that Na, Al, and Si all show solubility enhancement, the collection of polymeric species must involve all three elements. Thus, we propose that excess observed solubility is explained by the presence of polymerized aqueous silicate, aluminosilicate and Na-aluminosilicate species. This interpretation is supported by the fact that silica dimers were explicitly included in the solubility calculations. As shown in Fig. 5, the percentage of total calculated silica in dimers increases with temperature, and within ~50 °C of melting, dimers should account for nearly half of the calculated silica in solution. That additional polymeric species would be increasing in concert with silica dimers is sensible. The interpretation is also supported by experimental evidence for polymeric species in compositionally simpler systems, and similar systems but at higher *P* and *T*. It is now well established that, with rising *P* and *T*, monomeric $SiO_{2,aq}$ reacts in solution not only to progressively higher concentrations of $Si_2O_{4,aq}$ dimers (Zotov and Keppler, 2000, 2002; Newton and Manning, 2002, 2003), but also more polymerized species. For example, Newton and Manning (2008) inferred more extensive polymerization above 900 °C at 1 GPa. Formation of simple Al–Si species, likely dimers, has been documented at high *P* and *T* (Salvi et al., 1998; Manning, 2007), but thermodynamic data are insufficient to incorporate in our calculations. The observation that Na abundance is also strongly affected requires additional species involving this element. Mibe et al. (2008) report significant polymerization of dissolved silicates in the system K_2O–Al_2O_3–SiO_2–H_2O, though they limit their consideration to SiO_2 trimers and rings, and possible Al–Si oligomers; no evidence for oligomers involving alkali metal was reported. Although the data are insufficient on their own to establish the structure or stoichiometry of the proposed solute species, a mixture

Fig. 4. Variation in abundance of Si (a), Al (b), and Na (c) species with temperature near the melting point. Excess solubility indicates the presence of additional species that are in all cases and at all temperatures more abundant than those considered in the solubility calculations. These are interpreted to be polymerized species ("other"); these and silica dimers are shown in green, whereas monomeric species, ions and ion pairs are shown in blue. Melting point as in Fig. 2.

of simple dimers, trimers, and rings is likely. Given the alkaline pH, it is probable that the mixture includes both neutral and negatively charged clusters. Regardless, a key feature of the proposed species is that, unlike monomers and ion pairs, a fraction of the oxygen is in bridging positions (e.g., …Si–O–Si… and …Si–O–Al…), as indicated by in situ Raman spectroscopic studies (Mysen, 1998; Zotov and Keppler, 2000, 2002).

The relative abundance and composition of the inferred polymerized species at 580–635 °C is given in Table 3, and illustrated in Fig. 6. Despite the strong rise in bulk solubility over a narrow T interval (Fig. 2), the relative concentrations of monomeric species, ions and associated pairs of Si, Al and Na decrease from 32 to 21% as temperature rises from 580 to 620 °C. Polymeric species must increase commensurately. Extrapolation to the 1 GPa melting temperature (635 °C) suggests that the Si, Al, and Na in the vapor phase coexisting with the first hydrous melt are over 80% polymerized, and that polymer concentration is nearly 8 wt.%. The relative composition of the monomeric species remains essentially unchanged over this T interval, whereas the polymerized solute shows significant changes (Fig. 6). The silica dimer decreases in relative abundance as compared to more polymerized SiO_2. In addition, the participation of Na and Al in polymeric species increases. Both the unpolymerized and the polymerized portions of the solution are more silicic than albite stoichiometry, with molar Si/(Na + Al) >2.8 (compared to 1.5 in albite). Similarly, solutes are peralkaline, with Na/Al>1.1 for both the unpolymerized and polymerized fractions (the ratio in albite is 1). Both stoichiometric ratios become more albite-like as T rises.

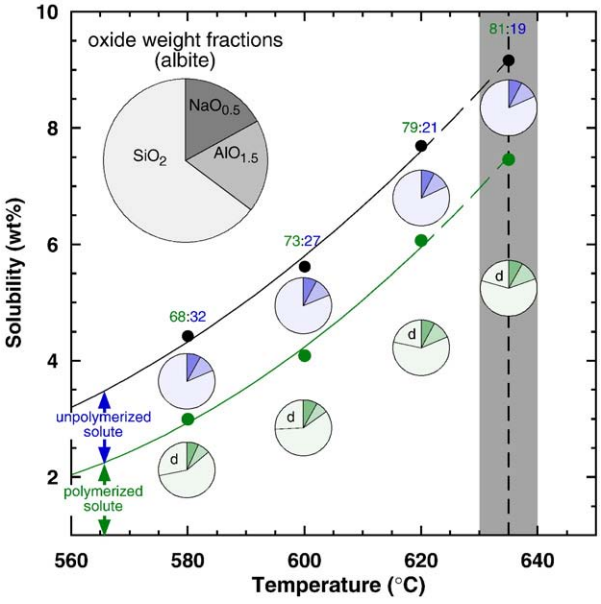

Fig. 6. Inferred variation in abundance and composition of polymerized and unpolymerized species with temperature near the melting point. Filled black circles and fitted curve show bulk solubility (as oxide wt.%); filled green circles and fitted curve show concentration of polymerized species. Melting point as in Fig. 2. The region labeled "unpolymerized solute" corresponds to calculated solubility, less silica dimers; the region labeled "polymerized solute" corresponds to calculated silica dimers plus the difference between calculated and observed solubility (Table 3). Fit curves were generated by assuming no excess solubility at 500 °C, and extrapolated to the melting temperature to obtain inferred melt-saturated solubility and fluid composition. Ratios above bulk solubility symbols indicate relative weights of polymerized (green) and unpolymerized (blue) solute, in %. Pie diagrams show relative concentrations of unpolymerized (blue) and polymerized (green) solute, in terms of oxide weight fractions ($NaO_{0.5}$, dark shading; $AlO_{1.5}$, intermediate; SiO_2, light). In the polymerized species diagrams, SiO_2 is subdivided into dimeric silica (d) and other silica (unlabeled). The example in upper left illustrates oxide fractions corresponding to albite stoichiometry. Both polymerized and unpolymerized solutes are more Si-rich and Na-rich than albite (see text).

4.5. Solute polymerization as a premelting effect

Recognition of the polymerization of silicate species dissolved in H_2O leads to a conceptual model linking mineral solubility, aqueous speciation and hydrothermal melting at high pressure (Fig. 7). At 1 GPa, the solute species >100 °C below the hydrothermal melting point are adequately modeled as a collection of neutral and deprotonated monomers ($SiO_{2,aq}$, $HSiO_3^-$, $HAlO_{2,aq}$), ions (Na^+, AlO_2^-) and simple complexes ($NaOH_{aq}$, $NaAlO_2$, $NaHSiO_3$). Silica dimers are present but their abundance is low (Fig. 5). As temperature rises isobarically to within ~100 °C of the melting point, these species are superseded in the solution by additional silica dimers, along with dimers and trimers involving combinations of Si, Al and Na (Na may also participate as an associated charge-balancing cation). The simple oligomers increase in abundance with continued rise in temperature, and likely interact to form yet more polymerized species as the melting point is approached. This leads to further rise in bulk solubility, as well as solubility of each individual element. Hydrothermal melting occurs at the point where the dissolved polymeric Si, Al–Si, and Na–Al–Si entities condense as they react with coexisting minerals and H_2O, forming more polymerized structures in a separate liquid phase with distinct physical and thermodynamic properties. Seen in this way, polymerization in the aqueous phase is a premelting

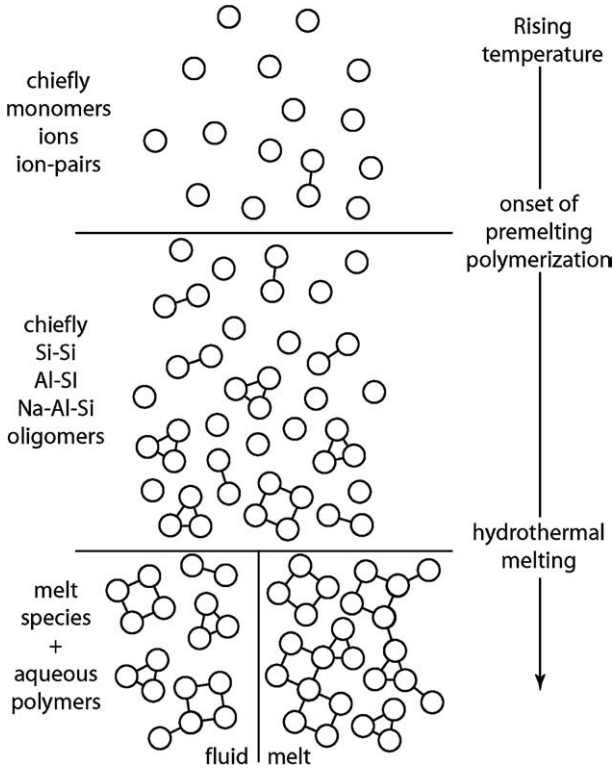

Fig. 7. Conceptual model of progressive polymerization of the aqueous phase in equilibrium with albite + paragonite + quartz, with isobaric temperature rise to the hydrothermal melting point. Circles represent Si, Al, and Na, lines bridging oxygens. (lines) Circles joined by lines represent dimers, trimers and other polymeric species. The appearance of excess solubility within ~100 °C of the melting temperature, and its increase as the melting point is approached, suggest that the aqueous phase experiences premelting polymerization, shown schematically by an increase in bridging oxygen positions. This yields dissolved polymeric species that react with minerals and condense to form a more polymerized hydrous silicate liquid when the melting point is reached. A corollary of the model is that H_2O-rich magmatic fluids coexisting with (or exsolved from) crystallizing magmas will be substantially polymerized. As a fluid equilibrated near the melting point moves, the elevated concentrations of polymeric species will promote metasomatic alteration of crustal rocks. Polymeric species provide energetic environments that are more favorable for otherwise insoluble elements, leading to mass transfer of refractory oxide components and helping to explain the presence of minerals bearing these constituents in veins and segregations.

effect that signals a system's proximity to the melting curve. Here, the term "premelting" is not synonymous with surface melting in a one component system (c.f., Dash, 1989), but instead refers to the formation of oxide clusters dissolved in the aqueous phase and becoming more melt-like as the solidus is approached. Premelting polymerization of dissolved silicate solutes can be seen as a process that lowers the energy barrier to silicate–liquid nucleation by producing the structural components which condense to form the melt phase. It is important to note that although there is debate about the extent of polymerization in hydrous albite, albite–quartz and other Na_2O–Al_2O_3–SiO_2 liquids (e.g., Burnham and Davis, 1974; Mysen et al., 1980; Mysen and Virgo, 1986; Kohn et al., 1989, 1994; Sykes and Kubicki, 1993, 1994; McMillan, 1994; Maekawa et al., 1998; Xu et al., 1998; Schmidt et al., 2000), the hydrous melts are in any case substantially more polymerized than the coexisting aqueous phase.

Support for this conceptual model can be found in the simple SiO_2–H_2O system, in which progressive polymerization of aqueous silica is observed as the temperature of hydrothermal melting is approached (Newton and Manning, 2008). Although polymerized silicate, aluminosilicate and alkali–aluminosilicate species have been recognized or proposed previously, a key insight gained from the present work is the rapid change in inferred extent of polymerization in the vicinity of the hydrothermal melting point, along with the relatively low temperature (500–620 °C), as compared to previous studies of polymerization in the aqueous phase (Mysen, 1998, 2007; Zotov and Keppler, 2000, 2002; Mysen and Armstrong, 2002; Newton and Manning, 2002, 2003, 2008; Mysen and Shang, 2003; Mibe et al., 2008).

Because our experiments were limited to 1 GPa, it is not clear whether the effect, if present, is limited to high pressure. In their study of the solubility of albite in H_2O at 500–700 °C, 0.20–0.85 GPa, Anderson and Burnham (1983) found that, along isotherms, SiO_2 concentrations approached or exceeded quartz solubility with rising P, and speculated that this was facilitated by increasing concentration of a solute complex having albite stoichiometry. At lower P (0.10–0.25 GPa), Woodland and Walther (1987) inferred the presence of Na–Al complexes in H_2O equilibrated with albite + paragonite + quartz at 350–500 °C. They considered the possibility that SiO_2 participated in the Na–Al complexes, but their data did not permit precise evaluation of the amount of Si involved. Studies of the solubility of albite + K feldspar + andalusite + quartz in aqueous chloride solutions at 600 and 650 °C, 0.2 GPa (Hauzenberger et al., 2002; Pak et al., 2003) considered alkali–Al and alkali–Si complexes, but found it unnecessary to invoke additional species to explain measured solubilities, consistent with the idea that the presence of alkali chloride in solution lowers the abundance of such species (e.g., Anderson et al., 1987). Thus, previous work hints at the possibility of Na–Al ± Si complexing might become more important with rising pressure. If so, premelting polymerization at 1 GPa may in part govern the appearance, at ~1.5 GPa, of a critical end-point in the system albite–H_2O (e.g., Shen and Keppler, 1997; Stalder et al., 2000; Manning, 2004; Hack et al., 2007).

Considering instead an isobaric cooling path at 1 GPa, the model implies that an aqueous fluid in a system that crosses the solidus contains Na–Al–Si–O clusters which persist to ~100 °C below the melt's freezing temperature. Though less polymerized than the melt, the aqueous phase is nevertheless more polymerized than has previously been inferred. The persistence of these polymeric fragments or clusters even after crystallization of the last melt means that magmatic fluids will carry more dissolved silicate as they migrate into country rocks (see below).

4.6. Implications for metasomatism

The excess solubility observed in the present study within ~100 °C of hydrothermal melting has important implications for mass transfer associated with crystallization of deeply emplaced magma bodies or crustal metamorphism. H_2O-rich magmatic fluids will contain high concentrations of alkalis and aluminosilicates, even after cooling to subsolidus T. The migration of such fluids down temperature and pressure gradients will produce more aluminous vein assemblages than has been previously appreciated. This could support the inference of a hydrothermal origin for some granophyric veins in and around igneous complexes (e.g., Czamanske et al., 1991). In addition, substantial mass transfer has been inferred at near-solidus conditions in high-grade Barrovian metamorphic rocks (e.g., Ague, 1994, 1997, 2003). However, in spite of their quantitative rigor, these studies have been challenged, in part because of the large fluxes of metamorphic fluids they seem to require (e.g., Yardley, 2009). The results of the present study help to reconcile these conflicting interpretations because the solubility enhancement afforded by polymerization will lead to substantially greater mass transfer by a given volume of fluid, all else being equal. As noted by Manning (2004), the presence of polymerized aluminosilicates in the fluid phase will also promote solubility and mobility of other elements that can substitute into the energetically favorable coordination environments, including many nominally insoluble elements. For example, Ti solubility increases systematically with dissolved Na-aluminosilicate (Antignano and Manning, 2008b; Manning et al., 2008). In general, deep metamorphic systems that encounter temperatures within ~100 °C of their solidus–even if they do not partially melt–can be expected to experience elevated mass transfer due to premelting polymerization in the aqueous phase.

5. Conclusions

1. Hydrothermal melting of albite + quartz occurs at 1 GPa, 635 ± 5 °C. The melting signal was robust because of the high water–rock ratios in the experiments, leading to slightly lower T than previously determined.
2. Bulk solubility of the invariant assemblage albite + paragonite + quartz in H_2O increases with T at 1 GPa, rising from ~1 to >8 wt.% at 350 to 620 °C. Individual elements display similar isobaric solubility increase with T.
3. Calculated solubility using extrapolated equilibrium constants for equilibria involving monomeric species, the silica dimer, ions and simple aqueous species yields good agreement with the experimental data at 350 to ~500 °C; however, at higher T the measured solubilities were greater than the predictions, and the discrepancy grew with approach to the hydrothermal melting point. All three elements show experimental concentrations in excess of those calculated.
4. The excess solubility is best interpreted as the progressive appearance of more polymerized solutes. The involvement of Si, Al, and Na requires that these polymeric complexes carry all three elements. The stoichiometries of individual species cannot be determined from this approach, but the bulk solubility requires that the polymerized solutes together have higher silica content, and higher Na/Al, than albite, $NaAlSi_3O_8$. Polymerized species represent more than 80% of the solute load at the hydrothermal melting point.
5. The observations support a simple conceptual model in which, with approach to the melting point, fluids in equilibrium with alkali aluminosilicate mineral assemblages polymerize to an increasing degree. This premelting effect, which may be characteristic of high pressure, is a precursor to melting in that it generates the simple polymeric clusters which may facilitate the eventual condensation of a hydrous silicate liquid with continued increase in T. Were monomers, ions and ion pairs the only structures in solution, hydrothermal melting would likely occur at different conditions, and the coexisting fluid phase would necessarily be much more dilute.
6. The existence of abundant aluminosilicate polymers in solution could promote substantial mass transfer by relatively small fluid volumes.

In addition, by providing energetically favorable coordination environments, this solute behavior may explain the transport and precipitation of insoluble oxide components in hydrothermal veins in metamorphic rocks or associated with cooling magmas in the middle and lower crust.

Acknowledgments

This work was supported by National Science Foundation grants EAR-0337170 and 0711521. We thank R. Newton, P. Tropper, A. Wohlers and D. Dolejs for discussions and assistance. The manuscript was completed while CEM was in residence at the Bayerisches GeoInstitute through the auspices of the Humboldt Foundation. Reviews by A. Hack and an anonymous reviewer improved the manuscript.

Appendix A. Supplementary data

Supplementary data associated with this article can be found, in the online version, at doi:10.1016/j.epsl.2010.01.044.

References

Ague, J.J., 1994. Mass-transfer during Barrovian metamorphism of pelites, south-central Connecticut. 1. Evidence for changes in composition and volume. Am. J. Sci. 294, 989–1057.
Ague, J.J., 1997. Crustal mass transfer and index mineral growth in Barrow's garnet zone, northeast Scotland. Geology 25, 73–76.
Ague, J.J., 2003. Fluid infiltration and transport of major, minor, and trace elements during regional metamorphism of carbonate rocks, Wepawaug Schist, Connecticut, USA. Am. J. Sci. 303, 753–816.
Anderson, G.M., Burnham, C.W., 1983. Feldspar solubility and the transport of aluminum under metamorphic conditions. Am. J. Sci. 283A, 283–297.
Anderson, G.M., Pascal, M.L., Rao, J., 1987. Aluminum speciation in metamorphic fluid. In: Helgeson, H.C. (Ed.), Chemical Transport in Metasomatic Processes. : NATO ASI Series C, vol. 218. Reidel, pp. 297–321.
Anderson, G.M., Castet, S., Schott, J., Mesmer, R.E., 1991. The density model for estimation of thermodynamic parameters of reactions at high temperatures and pressures. Geochim. Cosmochim. Acta 55, 1769–1779.
Antignano, A., Manning, C.E., 2008a. Apatite solubility in H_2O and H_2O–NaCl at 700 to 900 °C and 0.7 to 2.0 GPa. Chem. Geol. 251, 112–119.
Antignano, A., Manning, C.E., 2008b. Rutile solubility in H_2O, H_2O–SiO_2, and H_2O–$NaAlSi_3O_8$ fluids at 0.7–2.0 GPa and 700–1000 °C: implications for mobility of nominally insoluble elements. Chem. Geol. 255, 283–293.
Boettcher, A.L., Wyllie, P.J., 1969. Phase relationships in the system $NaAlSiO_4$–SiO_2–H_2O to 35 kilobars pressure. Am. J. Sci. 267, 875–909.
Bureau, H., Keppler, H., 1999. Complete miscibility between silicate melts and hydrous fluids in the upper mantle: experimental evidence and geochemical implications. Earth Planet. Sci. Lett. 165, 187–196.
Burnham, C.W., 1975. Water and magmas, a mixing model. Geochim. Cosmochim. Acta 39, 1077–1084.
Burnham, C.W., Davis, N.F., 1974. The role of H_2O in silicate melts: thermodynamic and phase relations in the system $NaAlSi_3O_8$–H_2O to 10 kilobars, 700° to 1100 °C. Am. J. Sci. 274, 902–940.
Caciagli, N.C., Manning, C.E., 2003. The solubility of calcite in water at 6–16 kbar and 500–800 °C. Contrib. Mineral. Petrol. 146, 275–285.
Chatterjee, N.D., 1972. The upper stability limit of the assemblage paragonite + quartz and its natural occurrences. Contrib. Mineral. Petrol. 34, 288–303.
Currie, K.L., 1968. On the solubility of albite in supercritical water in the range 400 to 600 °C and 750 to 3500 bars. Am. J. Sci. 266, 321–341.
Czamanske, G.K., Zientek, M.L., Manning, C.E., 1991. Low-K granophyres of the Stillwater Complex, Montana. Am. Mineral. 76, 1646–1661.
Dash, J.G., 1989. Surface melting. Comtemp. Phys. 30, 89–100.
Goldsmith, J.R., Jenkins, D.M., 1985. The hydrothermal melting of low and high albite. Am. Mineral. 70, 924–933.
Haar, L., Gallagher, J.S., Kell, G.S., 1984. NBS/NRC Steam Tables. Hemisphere, New York, p. 320.
Hack, A.C., Hermann, J., Mavrogenes, J.A., 2007. Mineral solubility and hydrous melting relations in the deep earth: analysis of some binary A–H_2O system pressure–temperature-composition topologies. Am. J. Sci. 307, 833–855.
Hauzenberger, C.A., Baumgartner, L.P., Pak, T.M., 2002. Experimental study on the solubility of the "model"-pelite assemblage albite + K-feldspar + andalusite + quartz in supercritical chloride-rich aqueous solutions at 0.2 GPa and 600 °C. Geochim. Cosmochim. Acta 65, 4493–4507.
Helgeson, H.C., Delany, J.M., Nesbitt, H.W., Bird, D.K., 1978. Summary and critique of the thermodynamic properties of rock-forming minerals. Am. J. Sci. 278-A, 1–229.
Hermann, J., Spandler, C., 2008. Sediment melts at sub-arc depths: an experimental study. J. Petrol. 49, 717–740.
Johnson, J.W., Oelkers, E.H., Helgeson, H.C., 1992. SUPCRT92: a software package for calculating the standard molal thermodynamic properties of minerals, gases, aqueous species, and reactions from 1 to 5000 bars and 0 to 1000 °C. Comput. Geosci. 18, 899–947.
Kessel, R., Ulmer, P., Pettke, T., Schmidt, M., Thompson, A.B., 2005. The water–basalt system at 4–6 GPa: phase relations and second critical endpoint in a K-free eclogite at 700 to 1400 °C. Earth Planet. Sci. Lett. 237, 873–892.
Kohn, S.C., Dupree, R., Smith, M.E., 1989. A multinuclear magnetic resonance study of the structure of hydrous albite glasses. Geochim. Cosmochim. Acta 53, 2925–2935.
Kohn, S.C., Smith, M.E., Dupree, R., 1994. Comment on "A model for H_2O solubility mechanisms in albite melts from infrared spectroscopy and molecular orbital calculations" by D. Sykes and J. D. Kubicki. Geochim. Cosmochim. Acta 58, 1377–1380.
Kracek, F.C., Neuvonen, K.J., 1952. Thermochemistry of plagioclase and alkali feldspars. Am. J. Sci. 250, 293–318.
Lin, H., 2001. Aqueous geochemistry at subduction zone conditions: experimental constraints. Unpublished Ph.D. Thesis, University of California, Los Angeles, 247 pp.
Luth, W.C., 1968. The influence of pressure on the composition of eutectic liquids in the binary systems sanidine silica and albite–silica. Carnegie Inst. Washington Yearbook 66, 480–484.
Luth, W.C., Jahns, R.H., Tuttle, O.F., 1964. The granite system at pressures of 4 to 10 kilobars. J. Geophys. Res. 69, 759–773.
Maekawa, H., Saito, T., Yokokawa, T., 1998. Water in silicate glass: ^{17}O NMR of hydrous silica, albite and $Na_2Si_4O_9$ glasses. J. Phys. Chem. B 102, 7523–7529.
Manning, C.E., 1994. The solubility of quartz in H_2O in the lower crust and upper mantle. Geochim. Cosmochim. Acta 58, 4831–4839.
Manning, C.E., 1998. Fluid composition at the blueschist–eclogite transition in the model system Na_2O–Al_2O_3–SiO_2–H_2O–HCl. Schweiz. Mineral. Petrogr. Mitt. 78, 225–242.
Manning, C.E., 2004. The chemistry of subduction-zone fluids. Earth Planet. Sci. Lett. 223, 1–16.
Manning, C.E., 2007. Solubility of corundum plus kyanite in H_2O at 700 °C and 10 kbar: evidence for Al–Si complexing at high pressure and temperature. Geofluids 7, 258–269.
Manning, C.E., Boettcher, S.L., 1994. Rapid-quench hydrothermal experiments at mantle pressures and temperatures. Am. Mineral. 79, 1153–1158.
Manning, C.E., Wilke, M., Schmidt, C., Cauzid, J., 2008. Rutile solubility in albite–H_2O and $Na_2Si_3O_7$–H_2O at high temperatures and pressures by in-situ synchrotron radiation micro-XRF. Earth Planet. Sci. Lett. 272, 730–737.
Marshall, W.L., Franck, E.U., 1981. Ion product of water substance, 0–1000 °C, 1–10, 000 bars. New international formulation and its background. J. Phys. Chem. Ref. Data 10, 295–304.
Marshall, W.L., Mesmer, R.E., 1984. Pressure–density relationships and ionization equilibria in aqueous solutions. J. Solution Chem. 13, 383–391.
McMillan, P.F., 1994. Water solubility and speciation models. Rev. Miner. 30, 131–156.
Mesmer, R.E., Marshall, W.L., Palmer, D.A., Simonson, J.M., Holmes, H.F., 1988. Thermodynamics of aqueous association and ionization reactions at high temperatures and pressures. J. Solution Chem. 17, 699–718.
Mibe, K., Kanzaki, M., Kawamoto, T., Matsukage, K.N., Fei, Y., Ono, S., 2007. Second critical endpoint in the peridotite–H_2O system. J. Geophys. Res. 112, B03201.
Mibe, K., Chou, I.M., Bassett, W.A., 2008. In situ Raman spectroscopic investigation of the structure of subduction-zone fluids. J. Geophys. Res. 113 (B04208), 1–8.
Mysen, B.O., 1998. Interaction between aqueous fluid and silicate melt in the pressure and temperature regime of the Earth's crust and upper mantle. N. Jb. Mineral. Abh. 172, 227–244.
Mysen, B.O., 2007. The solution behavior of H_2O in peralkaline aluminosilicate melts at high pressure with implications for properties of hydrous melts. Geochim. Cosmochim. Acta 71, 1820–1834.
Mysen, B.O., Armstrong, L., 2002. Solubility behavior of alkali aluminosilicate components in aqueous fluids and silicate melts at high pressure and temperature. Geochim. Cosmochim. Acta 66, 2287–2297.
Mysen, B.O., Shang, J., 2003. Fractionation of major elements between coexisting H_2O-saturated silicate melt and silicate-saturated aqueous fluids in aluminosilicate systems at 1–2 GPa. Geochim. Cosmochim. Acta 67, 3925–3936.
Mysen, B.O., Virgo, D., 1986. Volatiles in silicate melts at high pressure and temperature. 2. Water in melts along the join $NaAlO_2$–SiO_2 and a comparison of solubility mechanisms of water and fluorine. Chem. Geol. 57, 333–358.
Mysen, B.O., Virgo, D., Harrison, W.J., Scarfe, C.M., 1980. Solubility mechanisms of H_2O in silicate melts at high pressures and temperatures: a Raman spectroscopic study. Am. Mineral. 65, 900–914.
Newton, R.C., Manning, C.E., 2002. Solubility of enstatite + forsterite in H_2O at deep crust/upper mantle conditions: 4 to 15 kbar and 700 to 900 °C. Geochim. Cosmochim. Acta 66, 4165–4176.
Newton, R.C., Manning, C.E., 2003. Activity coefficient and polymerization of aqueous silica at 800 °C, 12 kbar, from solubility measurements on SiO_2-buffering mineral assemblages. Contrib. Mineral. Petrol. 146, 135–143.
Newton, R.C., Manning, C.E., 2008. Thermodynamics of SiO_2–H_2O fluid near the upper critical end point from quartz solubility measurements at 10 kbar. Earth Planet. Sci. Lett. 274, 241–249.
Paillat, O., Elphick, S.C., Brown, W.L., 1992. The solubility of water in $NaAlSi_3O_8$ melts: a re-examination of Ab–H_2O phase relationships and critical behavior at high pressures. Contrib. Mineral. Petrol. 112, 490–500.
Pak, T.M., Hauzenberger, C.A., Baumgartner, L.P., 2003. Solubility of the assemblage albite + K-feldspar + andalusite + quartz in supercritical aqueous chloride solutions at 650 °C and 2 kbar. Chem. Geol. 200, 377–393.
Pokrovskii, V.A., Helgeson, H.C., 1995. Thermodynamic properties of aqueous species and the solubilities of minerals at high pressures and temperatures: the system Al_2O_3–H_2O–NaCl. Am. J. Sci. 295, 1255–1342.
Salvi, S., Pokrovski, G.S., Schott, J.S., 1998. Experimental investigation of aluminum–silica aqueous complexing at 300 °C. Chem. Geol. 151, 51–67.

Schmidt, B.C., Reimer, T., Kohn, S.C., Behrens, H., Dupree, R., 2000. Different water solubility mechanisms in hydrous glasses along the Qz–Ab join: evidence from NMR spectroscopy. Geochim. Cosmochim. Acta 64, 513–526.
Shen, A., Keppler, H., 1997. Direct observation of complete miscibility in the albite–H_2O system. Nature 385, 710–712.
Shmulovich, K., Graham, C., Yardley, B., 2001. Quartz, albite and diopside solubilities in H_2O–NaCl and H_2O–CO_2 fluids at 0.5–0.9 GPa. Contrib. Mineral. Petrol. 141, 95–108.
Shock, E.L., Sassani, D.C., Willis, M., Sverjensky, D.A., 1997. Inorganic species in geologic fluids: correlations among standard molal thermodynamic properties of aqueous ions and hydroxide complexes. Geochim. Cosmochim. Acta 61, 907–950.
Stalder, R., Ulmer, P., Thompson, A.B., Günther, D., 2000. Experimental approach to constrain second critical end points in fluid/silicate systems: near-solidus fluids and melts in the system albite-H_2O. Am. Mineral. 85, 68–77.
Sverjensky, D.A., Shock, E.L., Helgeson, H.C., 1997. Prediction of the thermodynamic properties of aqueous metal complexes to 1000 °C and 5 kb. Geochim. Cosmochim. Acta 61, 1359–1412.
Sykes, D., Kubicki, J.D., 1993. A model for H_2O solubility mechanisms in albite melts from infrared spectroscopy and molecular orbital calculations. Geochim. Cosmochim. Acta 57, 1039–1052.
Sykes, D., Kubicki, J.D., 1994. Reply to the comment by S.C. Kohn, M.E. Smith, and R. Dupree on "A model for H2O solubility mechanisms in albite melts from infrared spectroscopy and molecular orbital calculations". Geochim. Cosmochim. Acta 58, 1381–1384.
Tropper, P., Manning, C.E., 2005. Very low solubility of rutile in H_2O at high pressure and temperature, and its implications for Ti mobility in subduction zones. Am. Mineral. 90, 502–505.
Tropper, P., Manning, C.E., 2007. The solubility of corundum in H_2O at high pressure and temperature and its implications for Al mobility in the deep crust and upper mantle. Chem. Geol. 240, 54–60.
Walther, J.V., Helgeson, H.C., 1977. Calculation of the thermodynamic properties of aquous silica and the solubility of quartz and its polymorphs at high pressures and temperatures. Am. J. Sci. 277, 1315–1351.
Wohlers, A., Manning, C.E., 2009. Solubility of corundum in aqueous KOH solutions at 700 °C and 1 GPa. Chem. Geol. 262, 326–333.
Woodland, A.B., Walther, J.V., 1987. Experimental determination of the solubility of the assemglage paragonite, albite, and quartz in supercritical H2O. Geochim. Cosmochim. Acta 51, 365–372.
Xu, Z., Maekawa, H., Oglesby, J.V., Stebbins, J.F., 1998. Oxygen speciation in hydrous silicate glasses: an oxygen-17 NMR study. J. Am. Chem. Soc. 120, 9894–9901.
Yardley, B.W.D., 2009. The role of water in the evolution of the continental crust. J. Geol. Soc. Lond. 166, 585–600.
Zotov, N., Keppler, H., 2000. In-situ Raman spectra of dissolved silica species in aqueous fluids to 900 °C and 14 kbar. Am. Mineral. 85, 600–604.
Zotov, N., Keppler, H., 2002. Silica speciation in aqueous fluids at high pressures and temperatures. Chem. Geol. 184, 71–82.